Chapter 14

Quantitative Motion Analysis in Two and Three Dimensions

Deborah J. Wessels, Daniel F. Lusche, Spencer Kuhl, Amanda Scherer, Edward Voss, and David R. Soll

Abstract

This chapter describes 2D quantitative methods for motion analysis as well as 3D motion analysis and reconstruction methods. Emphasis is placed on the analysis of dynamic cell shape changes that occur through extension and retraction of force generating structures such as pseudopodia and lamellipodia. Quantitative analysis of these structures is an underutilized tool in the field of cell migration. Our intent, therefore, is to present methods that we developed in an effort to elucidate mechanisms of basic cell motility, directed cell motion during chemotaxis, and metastasis. We hope to demonstrate how application of these methods can more clearly define alterations in motility that arise due to specific mutations or disease and hence, suggest mechanisms or pathways involved in normal cell crawling and treatment strategies in the case of disease. In addition, we present a 4D tumorigenesis model for high-resolution analysis of cancer cells from cell lines and human cancer tissue in a 3D matrix. Use of this model led to the discovery of the coalescence of cancer cell aggregates and unique cell behaviors not seen in normal cells or normal tissue. Graphic illustrations to visually display and quantify cell shape are presented along with algorithms and formulae for calculating select 2D and 3D motion analysis parameters.

Key words Cell motility, 2D motion analysis, 3D reconstruction, Cell migration, 3D data, 4D tumorigenesis model

1 Introduction

The importance of cell migration in developmental biology, immunity, and disease has oft been repeated [1–4]. Indeed, it is becoming increasingly apparent that basic cell motility, that is, crawling in the absence of chemoattractant or other directionally stimulatory signals, may be an inherent cellular property [5]. Molecular mechanisms that drive cell motility have been studied extensively in the model system *Dictyostelium discoideum* [6–10] as well as in the so-called professional migratory cells such as neutrophils [1, 11–14] and macrophages [15, 16]. Considerable attention has also been focused on cell migration in the context of metastatic cancer [17–20] and understandably so since metastasis is the primary cause of death from this disease [21–23].

Ray H. Gavin (ed.), *Cytoskeleton: Methods and Protocols*, Methods in Molecular Biology, vol. 1365,
DOI 10.1007/978-1-4939-3124-8_14,

Basic cell motility may be modulated by chemotactic and haptotactic signals [24]. Hence, the failure of certain mutants to respond to an exogenous signal may actually be due to a mutation in the basic motility apparatus rather than a mutation in a signal transduction pathway [25] and this important distinction can only be made using appropriate quantitative methods. In addition, different migratory behaviors are manifested on 1D [3], 2D [3, 26] and 3D surfaces [27] due to physical properties of the substrate [27, 28], interactions between the substrate components and cell adhesion receptors [29], and the activity of extracellular proteases such as the metalloproteinases that degrade or remodel the matrix [30]. Again, deciphering the underlying mechanisms responsible for these characteristics requires accurate quantitation. It likewise is important to know the specific motility defects of abnormally behaving immune cells [24, 31, 32] in order to accurately diagnose the disease and provide successful treatment. Finally, it should be noted that although transwell assays are widely used to assay motility and chemotactic defects [33–35], they may not distinguish between chemotaxis and chemokinesis, provide only a limited amount of all-or-none information and no quantitative information on cytoskeletal dynamics or mechanisms of cell migration.

The aforementioned points speak to the need for high resolution 2D and 3D quantitative methods in which cell shape changes mediated by pseudopod or lamellipod dynamics [24, 36, 37], invadopodia [38, 39], podosomes [40, 41] and/or filopodia [37, 42] are analyzed in order to distinguish normal from aberrant motility and normal chemotaxis or other forms of directed motility on one hand from directed crawling that has been dampened or obliterated by signal transduction deficiencies on the other. Here we will describe high-resolution 2D and 3D methods for motion analysis of individual cells. We include protocols for 2D motion analysis of basic cell motility as well as chemotaxis on a 2D substrate, 3D motion analysis of basic cell motility and reconstruction on a 2D substrate and finally, 3D motion analysis of basic cell motility and reconstruction in a 3D matrix (i.e., 4D). As an example of the validity of this approach, we will show how high-resolution quantitation of cell motility led to the discovery in the model system *Dictyostelium discoideum* that upregulation of *lpten*, a homolog of *ptenA* that is, in turn, an ortholog of the human *PTEN* mutated in many human cancers, rescues defects in *ptenA*$^-$ mutants, raising the possibility of a new stratagem for cancer therapy [43]. In addition, accurate quantitation of cell shape changes in basic cell motility as well as in chemotaxis has provided insights into human diseases [31, 44] and, as we show here, can be used to evaluate coalescence of cancer cells, cell-cell interactions within the tumor microenvironment as well as effects of potential cancer treatments [41].

2 Materials

2.1 Culturing Dictyostelium discoideum

1. *D. discoideum* wild-type and mutant strains, as well as many plasmids, can be obtained from the Dictybase Stock Center. (http://www.dictybase.org/StockCenter/StockCenter.html).
2. HL-5 nutrient growth media supplemented with the appropriate antibiotics for transformed strain selection (http://dictybase.org).
3. Amoebae maintained at the low-log phase of growth (~2×10^6 cells/mL in HL-5) (*see* **Note 1**).

2.2 Development of D. discoideum for Basic Cell Motility and Chemotaxis Assays

1. BSS: 20 mM KCl, 2.5 mM $MgCl_2$, 20 mM KH_2PO_4, 5 mM Na_2HPO_4 (pH 6.4), 0.34 mM streptomycin sulfate, filter sterilized [22, 23].
2. HAB040700 nitrocellulose filters (Millipore, Billerica, MA, USA).
3. Millipore support filters (catalog AP1004700; www.millipore.com).
4. Humidified incubation chamber at 22 °C.
5. cAMP: 1 mM stock solution of adenosine 3′,5′-cyclic monophosphate (cAMP; Sigma-Aldrich, Inc. http://www.sigmaaldrich.com) diluted in BSS and frozen until use.

2.3 Isolation of Primary Human PMNs for Basic Cell Motility and Chemotaxis Assays

1. 10 mL whole venous blood drawn from healthy donors using IRB-approved informed consent protocols into blood collection tubes coated with anticoagulant, preferably EDTA for use with Polymorphprep. Heparin-coated tubes are not recommended for use with Polymorphprep.
2. Polymorphprep Axis Shield Density Gradient Media (www.cosmobiousa.com) for separation of neutrophils from whole blood.
3. Hepes-buffered Hanks' balanced salt solution (H-HBSS) with 1.26 mM $CaCl_2$ and 0.49 mM $MgCl_2$ (Life Technologies, Carlsbad, CA), pH 7.4 and 10 mM Hepes.
4. Centrifuge capable of 400–900 × *g* forces at room temperature with the option of no-brake deceleration.
5. *N*-formyl peptide (fMLP): 500 μM stock solution of *N-formyl-met*-leu-phe (Sigma-Aldrich, Inc.) in DMSO frozen until use.

2.4 Culturing Cell Lines

1. Laboratory personnel who have contact with cells, tissue, and/or blood products, particularly those of human origin, should be trained in the proper use of personal protective equipment (PPE) and the safe handling of material that may harbor bloodborne pathogens (*see* **Note 2**).
2. Certified biological safety cabinet, biohazardous waste decontamination, and biohazardous waste disposal systems.

3. Cell culture media: Dulbecco's modified Eagle's medium (DMEM), RPMI 1640, (Life Technologies, Carlsbad, CA, http://www.lifetechnologies.com) or supplier's media recommendation.
4. Fetal bovine serum (FBS, Atlanta Biologicals https://www.atlantabio.com/) (*see* **Note 3**).
5. Penicillin/streptomycin mixture (Life Technologies, Carlsbad, CA, http://www.lifetechnologies.com).
6. DPBS (Dulbecco's phosphate-buffered saline; Life Technologies, Carlsbad, CA http://www.lifetechnologies.com) without magnesium and without calcium for cell dissociation: 2.67 mM potassium chloride (KCl), 1.47 mM potassium phosphate monobasic (KH_2PO_4), sodium chloride (NaCl), and sodium phosphate dibasic ($Na_2HPO_4 \cdot 7H_2O$).
7. Trypsin-0.25 % EDTA with phenol red (Life Technologies, Carlsbad, CA, http://www.lifetechnologies.com).
8. CO_2 incubator at 37 °C and 5 % CO_2 (http://www.thermofisher.com/en/home.html).
9. Tissue culture flasks for cell culturing (http://www.usascientific.com/).

2.5 Culturing Cells from Tissue

1. DMEM/F12, M199, and/or RPMI 1640 (Life Technologies, Carlsbad, CA, http://www.lifetechnologies.com).
2. Horse serum and fetal calf serum (Life Technologies, Carlsbad, CA, http://www.lifetechnologies.com).
3. Epidermal growth factor human (EGF) (Sigma-Aldrich, St. Louis, MO, http://www.sigmaaldrich.com).
4. Hydrocortisone (Sigma-Aldrich, St. Louis, MO, http://www.sigmaaldrich.com).
5. Insulin (Sigma-Aldrich, St. Louis, MO).
6. Cholera toxin (Sigma-Aldrich, St. Louis, MO).
7. Penicillin/streptomycin (Gemini Bio-products).
8. 6-Well plates (Fisher Scientific, http://www.fishersci.com).
9. Sterile scissors, scalpels, and forceps.
10. CO_2 incubator at 37 °C and 5 % CO_2.

2.6 Preparation of Matrigel Cultures in Petri Dishes

1. Aliquoted Matrigel matrix (Becton Dickinson Bioscience, Franklin Lakes, NJ) stored at −20 °C (*see* **Note 4**).
2. Chilled pipette tips.
3. Chilled 35 mm and/or 65 mm plastic Petri dishes with glass insert in dish bottom (InVitro Scientific, www.invitrosci.com).

4. For 3D experiments, the Petri dishes may have to be modified. Modifications require sharp scissors sterilized in 100 % ethanol to trim the height of the dish bottom (*see* **Note 5**).
5. Modified Petri dish lid for use with DIC optics in 3D experiments (*see* **Note 6**).

2.7 2D Experiment on 2D substrate

1. Upright or inverted microscope (depending on the chamber used) equipped with phase or bright-field optics and 10–40× objectives.
2. When working with cell lines, tissues, and/or long-term experiments with immune cells isolated from freshly drawn blood, the microscope should be fitted with environmental controls or contained within a CO_2 incubator at 37 °C and 5 % CO_2.
3. Sony XCD-V50 1/3-type Progressive Scan IT CCD camera (or comparable) with a IEEE1394B high-speed digital interface that operates at 60 fps and 640×480 resolution, with C-mount and controlled by FireWire compatible software such as FireI (www.unibrain.com), Adobe Premiere®, QuickTime Pro®, iStopMotion, or iMovie.
4. Sykes-Moore perfusion chamber (Bellco Glass, Inc., http://www.bellcoglass.com) with 2.5 mm gasket, holder, and 25 mm #2 cover slips coupled to programmable pumps to assay basic cell motility, to assay response to global exposure to chemoattractant or to generate a dynamic gradient of temporal waves [46–48] (Fig. 1a).
5. For perfusion with the Sykes-Moore chamber, two pieces of Tygon tubing (1/16 in. ID), each connected to a 21-gauge needle via a luer lock for inlet and outlet ports and a 60 cm^3 syringe connected to the other end of the inlet tubing via a luer fitting (Fig. 1a, b).
6. For perfusion experiments, NE-1000 Multiphase Programmable Pumps (New Era Pump Systems, Farmingdale, NY) [49, 50] or other continuous pump system that does not introduce oscillations (Fig. 1b).
7. For quantifying the response of single cells to chemoattractant: Dunn chamber (http://www.hawksley.co.uk/), Zigmond chamber (Fig. 1c, d). (http://www.neuroprobe.com/products/zigmond.html), or modified Zigmond chamber [44, 51].
8. Single cells can also be imaged in gradients of chemoattractant generated in a microfluidic device [10, 52–54]. Various perfusion and chemotaxis chambers are also available from Ibidi (www.ibidi.com).
9. Coated cover slip within a Petri dish for mammalian cells (Fig. 1e).
10. An environmental chamber if pH and temperature need to be regulated; alternatively, microscope can be housed within a 37 °C, 5 % CO_2 incubator (Fig. 1f).

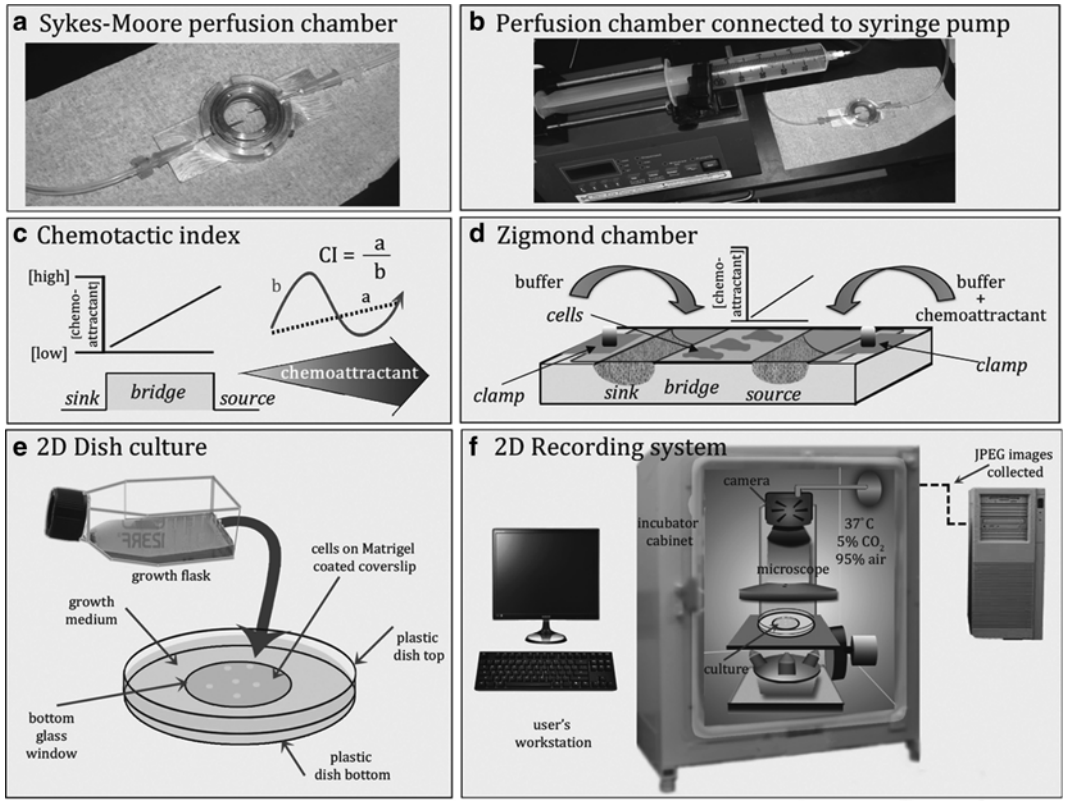

Fig. 1 Methods for 2D motion analysis of cells crawling on a 2D substrate. (*a*) The assembled Sykes-Moore perfusion chamber with inlet and out tubes inserted into their respective ports. (*b*) The Sykes-Moore perfusion chamber connected to a 60 cm^3 syringe containing the perfusion solution and placed in a programmable syringe pump. (*c*) Diagram of the gradient of chemoattractant that forms by diffusion across the bridge of the Zigmond chamber and the method for calculating the chemotactic index (CI). (*d*) Diagram of the Zigmond chemotaxis chamber. Cells are attached to the cover slip that is inverted over the bridge. Buffer is placed in the "sink" trough and buffer plus chemoattractant in the "source" trough. (*e*) Cells can be spread onto a thin coat of Matrigel or other matrix cast onto the glass window (cover slip) inserted into the bottom of a Petri dish for 2D analysis of mammalian cells crawling on a 2D substrate. (*f*) In cases requiring environmental regulation, image acquisition can be performed on a microscope with camera housed in an incubator

11. Dedicated acquisition computer capable of storing hundreds of gigabytes of data.
12. Motion analysis software such as ImageJ (http://imagej.nih.gov/ij/) or J3D-DIAS4.1 (*see* **Note 7**).

2.8 3D Experiment on a 2D substrate

1. Short-working-distance perfusion chamber such as the one available from Harvard Apparatus (http://www.harvardapparatus.com) or from Life Imaging Services (http://www.lis.ch/download/LIS_Ludin_Chamber_v8.pdf).
2. Microscope equipped with differential interference (DIC) optics, high numerical aperture objectives, high numerical aperture condenser, and motorized stage capable of moving

the focus through 10–20 μm in 2–3 s every 4–5 s (*see* **Note 8**) for rapidly moving cells such as *D. discoideum* and PMNs.

3. Environmental chambers are required to maintain temperature and pH for long-term imaging of mammalian cells. Alternatively, a microscope may be housed within a 37 °C, 5 % CO_2 incubator (*see* **Note 9**).
4. Digital camera controlled by video acquisition software such as the Zeiss AxioCam MRc5 and Laser Vision 6 software as described in **item 3**, Subheading 2.7, synchronized with the LED light engine and motorized stage.
5. A computer capable of running Microsoft Windows XP, equipped with serial ports (RS-232) to control the microscope *Z*-axis stepper motor, a firewire port (IEEE 1394) to capture images from the AxioCam MRc5 camera, and a storage disk capable of storing hundreds of gigabytes of data.
6. Software for 3D reconstruction (*see* **Note 7**).

2.9 3D Experiment on a 3D substrate

1. Cell cultures embedded in Matrigel in modified Petri dishes (Fig. 2a) as described in Subheading 2.6, **Notes 5** and **6**.
2. Microscope equipped with differential interference contrast (DIC) optics, programmable motorized stage, 20× or 40× long-working-distance objectives and LED light engine (*see* **Note 10**) contained within a 37 °C, 5 % CO_2 incubator or other means of regulating temperature and pH for 30 days or more of continual imaging (Fig. 2b).
3. Digital camera controlled by video acquisition software such as the Zeiss AxioCam MRc5 and Laser Vision 6 software, synchronized with the LED light engine and motorized stage.
4. A computer capable of running Microsoft Windows XP, equipped with serial ports (RS-232) to control the microscope *Z*-axis stepper motor, a firewire port (IEEE 1394) to capture images from the AxioCam MRc5 camera, and a storage disk capable of storing hundreds of gigabytes of data.
5. Software for 3D reconstruction (*see* **Note 7**).

3 Methods

3.1 Preparation of D. discoideum amoebae for 2D Analysis of Basic Motile Behavior and Chemotaxis

1. Harvest 5×10^7 cells in the low log phase of growth (~2×10^6 cells/mL), wash three times in BSS, and disperse on a nitrocellulose filter supported by two Millipore pre-filters pre-saturated with BSS. Incubate in a humidified chamber at 22 °C until the onset of aggregation [55] when motility and chemotactic responsiveness peak [55, 56]. Wash cells from the filter pads and dilute to 3×10^4 cells/mL (*see* **Note 10**) for inoculation into chamber.

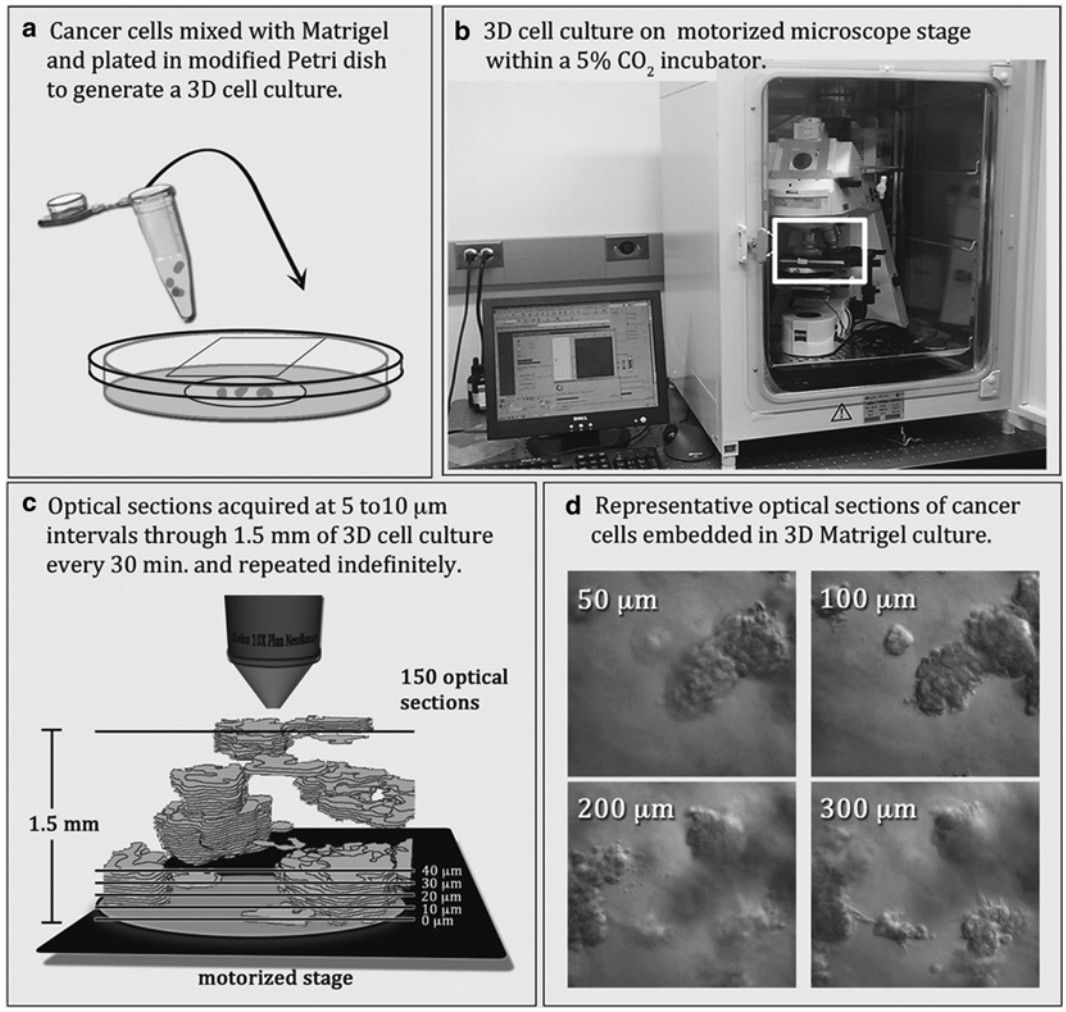

Fig. 2 Methods for 3D motion analysis of cells crawling on a 3D substrate. (*a*) Modified Petri dish for 3D analysis of cells embedded in a 3D matrix. Cells are mixed with Matrigel and plated onto a glass window in the bottom section of the Petri dish that has been trimmed to fit within the allowable working distance of the microscope. A glass window in the lid is necessary to achieve optical sections using DIC microscopy. (*b*) Microscope fitted with DIC optics and a motorized stage housed inside a 5 % CO_2, 37 °C incubator for long-term imaging of living cells in 3D cultures. Camera and motor are synchronized by controlling software. A timer regulates the LED light so that the specimen is only illuminated during the 45 s in which the z-series is actively being acquired. The *white box* indicates the area of the stage that is diagrammed at a larger scale in (*c*). (*c*) Diagrammatical summary of optical sectioning using DIC microscopy. A typical z-series of 150 optical sections is acquired through 1.5 mm of Matrigel matrix at 5–10 μm increments. (*d*) Representative optical sections through a culture of aggregating cancer cells embedded in a 3D Matrigel matrix. The level of each section is given in the upper left hand corner of each panel

2. Mutant *Dictyostelium* strains may be defective in cAMP signaling and cAMP induced gene expression, and therefore require exogenously applied pulses of cAMP in order to become motile and/or chemoresponsive [48]. To exogenously pulse cells,

harvest *D. discoideum* amoebae at the low log phase of growth, wash in BSS and resuspend at a density of 2×10^7 cells/mL in BSS. Maintain the flask containing the cell suspension on a rotary shaker at 180 rpm for 1 h. Cells are then pulsed by programming the NE-1000 Pumps to deliver 80 nM cAMP (final) from a 10 cm^3 syringe every 6 min for 6 subsequent hours [43, 48, 57]. At the completion of pulsing, cells are pelleted, washed in BSS, and diluted to 3×10^4 cells/mL for inoculation into a chamber.

3. For analysis of basic motile behavior, inoculate 1.1 mL of the dilute cell suspension into a Sykes-Moore perfusion chamber. Allow cells to adhere to the cover slip for 5–10 min, seal the chamber, and insert inlet and outlet needles into the respective ports. Connect inlet tube to a 60 cm^3 syringe filled with BSS and insert the syringe into a pump programmed to deliver 4 mL/min (Fig. 1a; *see* **Notes 10** and **11**).
4. For analysis of chemotaxis, streak 20 μL of the dilute cell suspension across the center of a clean 24×30 mm cover slip and allow 5 min for the cells to adhere. Invert the cover slip so that the cells contact the bridge then lightly fasten the clamps. Carefully pipette 55–60 μL of BSS into one trough (sink) and 55–60 μL of 10^{-6} M cAMP (source) into the other trough. Chamber assembly is diagrammed in Fig. 1d.

3.2 Preparation of Human Primary Polymorphonuclear Neutrophils (PMNs) for 2D Analysis of Basic Motile Behavior and Chemotaxis on a 2D Substrate

1. Whole venous blood is drawn into a blood collection tube coated with anticoagulant. The tube is gently inverted several times, brought to room temperature by gently rocking for about 30 min and 5 mL of blood is layered onto the top of 5 mL of Polymorphprep, also at room temperature, in a 15 mL Falcon centrifuge tube according to the manufacturer's instructions [49].
2. Centrifuge at room temperature for 30–35 min at $500 \times g$ with no brake.
3. The PMN band is collected, washed in H-HBSS by centrifugation at $400 \times g$ for 10 min, and resuspended to a concentration of 1.5×10^6 cells/mL in H-HBSS. Brake can be used during washing steps.
4. Inoculate into the Sykes-Moore perfusion chamber for motion analysis of basic motile behavior as described in Subheading 3.1, **step 3**, using H-HBSS as the perfusion buffer (Fig. 1a, b).
5. Inoculate into a chemotaxis chamber for motion analysis of chemotaxis as described in Subheading 3.1, **step 4**, using H-HBSS as the sink buffer and H-HBSS plus 0.1 μM fMLP as the chemoattractant in the source trough as illustrated in Fig. 1d.

3.3 Preparation of Cell Lines for 2D Analysis of Basic Motile Behavior on a 2D Substrate

1. Using a sterile, pre-chilled pipet tip, distribute 50 μL/cm^2 of ice-cold Matrigel onto the glass insert of a pre-chilled Petri dish, taking care not to introduce bubbles.
2. Incubate the Petri dish for 30 min at 37 °C.
3. Dissociate cells from tissue culture flask, resuspend in media, wash, resuspend in fresh media, and count.
4. Withdraw the volume required to yield 5×10^5 cells, adjust to 100 μL, and spread onto the pre-coated, gelled Matrigel coat.
5. Incubate for 30 min to allow cells to attach.
6. Add 1–3 mL of appropriate media to the dish.
7. Place preparation on the stage of the 2D microscope and begin image acquisition.

3.4 Image Capture and Outlining in 2D

1. For *D. discoideum* or for short-term recording of PMNs, place cells in the appropriate chamber on the stage of microscope equipped with phase optics and a camera controlled by software. Set the time interval and duration of experiment.
2. For mammalian cells, place the chamber on a microscope within a 37 °C, CO_2 incubator or in an environmental chamber.
3. Images are saved as a series of sequential JPEG files that can be opened in J3D-DIAS4.1 and saved in native format (Fig. 3a).
4. Imaging processing can facilitate automatic outlining (Fig. 3b) (*see* **Note 12**).
5. The edge of cells can be automatically detected in each frame employing a grayscale threshold algorithm (Fig. 3c).
6. The perimeter is converted to a mathematically precise beta-spline replacement image [58–61] and the centroid, or geometric center [59–61], at each time point (Fig. 3d) is determined (*see* **Note 13**).

3.5 2D Cell Movement and Shape Parameters

1. Cell motility parameters can be computed over time based on the changing position of the centroid [59–62] (Table 1a; Figs. 4d and 5b) and cell shape parameters can be quantified from the beta spline replacement images (Table 1b; *see* **Notes 14–16**).
2. The "chemotactic index" is computed as the net distance moved towards the source of chemoattractant divided by the total distance the cell migrated [63, 64] (Fig. 1c).
3. Cell shape changes can be evaluated by "unwrapping" and stacking. (Fig. 3b) Polar coordinates are converted to rectangular coordinates and stacked with each unwrapped perimeter having a lower offset than the previous one. This display accentuates the position and frequency of protrusions over time and therefore is particularly useful in determining cytoskeletal contributions to lamellipodial behavior [24, 36]

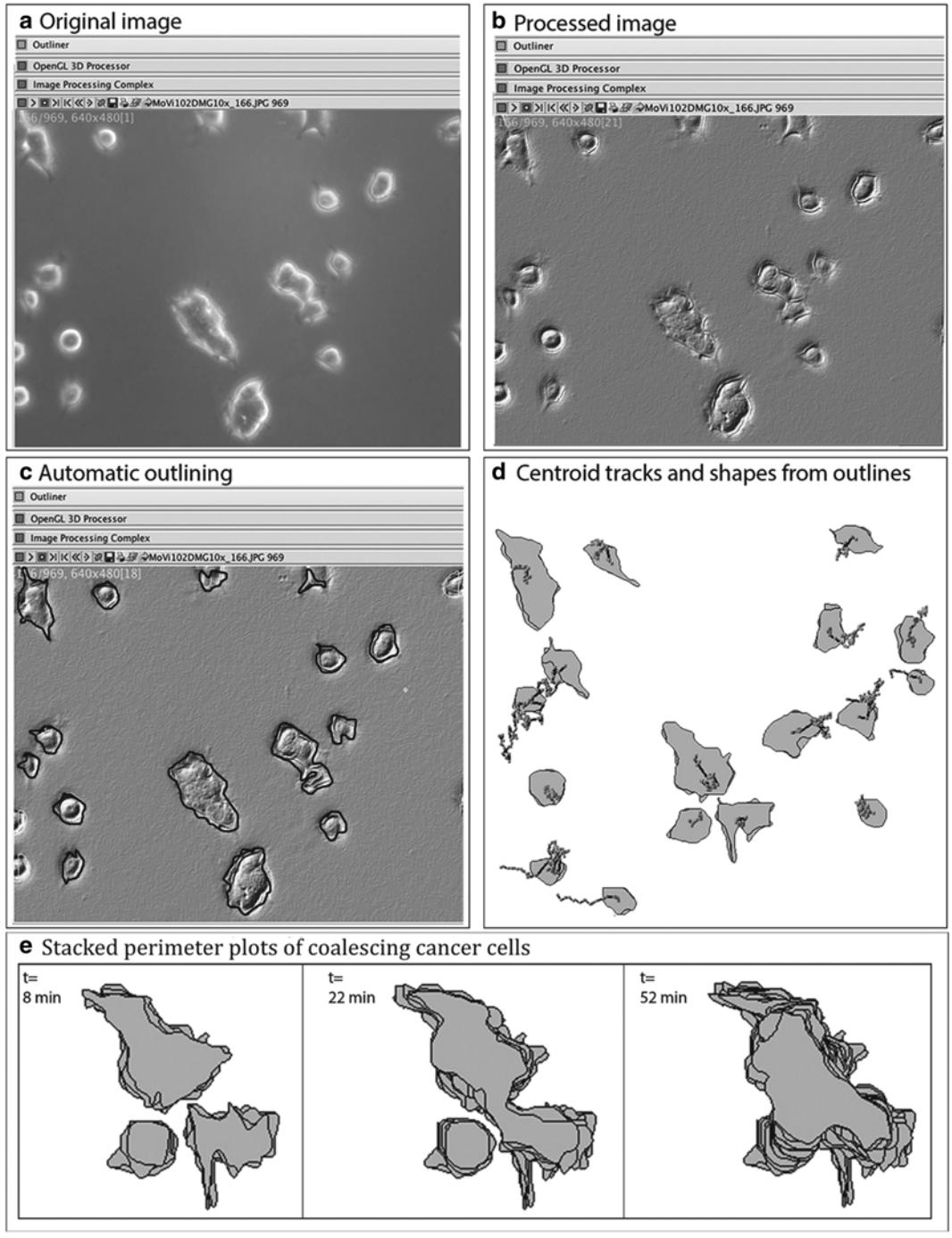

Fig. 3 2D automatic outlining, path and shape generation in cancer cells crawling on top of a 2D, thin coat of matrix. (*a*) Original phase image. (*b*) The image can be processed to facilitate automatic outlining. (*c*) Automatic outlining. (*d*) Centroid tracks and shapes generated from the outlines. (*e*) Stacked perimeter plots of coalescing cancer cells. Time is indicated in the *upper left hand corner*

Table 1
2D motility and shape parameters

A. Centroid-based 2D motility parameters														
Object	Frames	Time (min)	Total elapsed time (min)	Total path length (μm)	Net path length (μm)	Direct. total	Direct. upward	Direct. right	Speed (μm/min)	Direction (deg)	Direction change (deg)	Accel. (μm/sq min)	Persist. (μm/min deg)	Axis tilt (deg)
1	1–33	0.000–64.000	64	68.63	8.48	0.12	0.04	0.12	0.80	228.2	48.0	0.14	0.15	28.0
2	1–52	0.000–102.000	102	110.66	15.56	0.14	−0.08	0.12	0.69	297.7	40.8	0.19	0.13	333.0
3	1–102	0.000–202.000	202	137.61	10.80	0.08	−0.02	0.08	0.42	225.8	48.9	0.13	0.09	329.0
4	1–20	0.000–38.000	38	32.86	18.88	0.58	0.40	−0.41	0.76	135.5	70.5	0.06	0.22	339.6
5	1–16	0.000–30.000	30	21.19	3.78	0.18	−0.04	0.18	0.58	259.1	54.2	0.06	0.11	331.0
6	1–102	0.000–202.000	202	287.43	57.39	0.20	0.17	0.10	0.99	203.8	51.7	0.21	0.17	347.5
7	1–16	0.000–30.000	30	36.69	23.98	0.65	−0.19	0.63	1.15	292.1	74.3	0.07	0.31	337.1
8	1–102	0.000–202.000	202	237.02	36.95	0.16	0.14	0.08	0.83	210.5	50.0	0.18	0.16	342.5
9	1–16	0.000–30.000	30	61.53	13.43	0.22	−0.18	0.12	1.67	282.9	58.1	0.22	0.48	20.9
10	1–102	0.000–202.000	202	199.59	17.87	0.09	−0.05	−0.08	0.74	148.4	49.6	0.13	0.16	332.6

11	1–73	0.000–144.000	144	165.17	14.98	0.09	0.07	−0.06	0.80	49.1	49.4	0.17	0.16	319.3
12	1–102	0.000–202.000	202	165.93	8.74	0.05	0.05	−0.02	0.57	142.0	50.7	0.13	0.12	318.7
13	1–102	0.000–202.000	202	171.37	18.15	0.11	−0.09	0.06	0.67	311.3	59.9	0.09	0.16	318.6
14	1–11	0.000–20.000	20	32.73	6.56	0.20	−0.14	0.15	0.93	276.8	38.4	0.41	0.23	345.2
15	1–26	0.000–50.000	50	49.23	13.43	0.27	−0.21	−0.17	0.65	41.4	44.0	0.16	0.10	326.4
16	1–82	0.000–162.000	162	161.33	36.84	0.23	0.00	0.23	0.84	284.2	60.9	0.08	0.22	342.4
17	1–39	0.000–76.000	76	62.32	47.64	0.76	−0.07	0.76	0.74	274.8	68.1	0.05	0.20	312.5
19	21–102	40.000–202.000	162	90.32	24.27	0.27	−0.23	−0.14	0.41	21.7	55.0	0.07	0.07	7.1
20	25–102	48.000–202.000	154	110.23	12.85	0.12	−0.08	−0.08	0.52	49.1	56.2	0.10	0.13	316.1
21	25–102	48.000–202.000	154	178.85	12.32	0.07	0.07	−0.01	0.95	143.3	61.8	0.11	0.24	355.9
23	52–102	102.000–202.000	100	88.20	5.06	0.06	0.05	−0.02	0.73	9.5	61.1	0.08	0.22	326.8
26	74–102	146.000–202.000	56	44.57	2.44	0.06	0.00	0.06	0.58	301.9	52.5	0.11	0.16	331.0
			MEAN	114.2	18.7	0.2	0.0	0.1	0.8	190.4	54.7	0.1	0.2	289.1
			± S.D.	73.6	14.3	0.2	0.1	0.2	0.3	102.7	9.1	0.1	0.1	110.6

(continued)

Table 1
(continued)

B. 2D shape parameters

Object	Frames	Time (min)	Total elapsed time (min)	Maximum length (μm)	Mean width (μm)	Area (sq μm)	Per. (μm)	Rnd (%)	Mean radial length (μm)	Radial deviation (%)	Mean Conv. (deg)	Mean Conc. (deg)	Pos. flow (%)	Neg. flow (%)
1	1–33	0.000–64.000	64	41.8	19.6	823.4	119.9	71.9	16.4	18.9	725.5	365.5	12.8	13.0
2	1–52	0.000–102.000	102	69.2	21.6	1493.9	189.9	52.3	23.3	31.2	1058.0	698.0	9.4	10.5
3	1–102	0.000–202.000	202	28.1	12.4	344.1	75.1	78.1	10.8	18.8	518.5	1585	10.4	11.8
4	1–20	0.000–38.000	38	31.9	13.9	439.5	87.2	75.1	12.3	19.0	563.4	203.4	12.7	15.2
5	1–16	0.000–30.000	30	35.2	18.3	640.4	101.9	77.7	14.4	17.1	601.8	241.8	9.9	12.0
6	1–102	0.000–202.000	202	32.9	13.9	451.8	90.2	72.2	12.4	19.7	620.2	260.2	18.2	20.5
7	1–16	0.000–30.000	30	22.8	10.7	243.4	61.9	81.9	9.0	17.0	473.7	113.7	20.3	19.4
8	1–102	0.000–202.000	202	23.6	10.7	254.2	63.6	79.8	9.2	18.3	493.2	136.8	20.3	25.1
9	1–16	0.000–30.000	30	35.7	16.0	571.1	100.5	71.4	13.8	20.0	625.3	265.3	20.8	24.2
10	1–102	0.000–202.000	202	54.9	20.4	1117.9	148.8	65.8	19.7	25.1	819.5	466.7	9.9	10.7
11	1–73	0.000–144.000	144	88.2	24.5	2152.7	236.4	49.1	28.8	33.6	1117.7	762.7	9.9	9.7

12	1–102	0.000–202.000	202	27.7	14.1	394.2	78.8	78.8	11.3	15.4	565.4	205.4	14.5	16.8
13	1–102	0.000–202.000	202	24.8	12.2	307.0	67.4	84.2	10.0	15.7	466.2	106.2	15.3	18.0
14	1–11	0.000–20.000	20	51.2	16.9	862.4	165.0	41.5	17.5	30.2	1015.5	655.5	13.6	15.2
15	1–26	0.000–50.000	50	25.7	15.0	387.5	72.6	92.0	11.1	9.2	440.0	80.0	12.6	17.3
16	1–82	0.000–162.000	162	26.8	11.8	314.3	74.3	75.7	10.3	19.5	567.8	207.8	17.7	20.4
17	1–39	0.000–76.000	76	24.2	11.8	286.0	66.7	81.2	9.6	17.1	474.0	114.0	14.3	17.5
19	21–102	40.000–202.000	162	35.6	17.5	621.8	98.5	81.4	14.2	17.5	585.9	225.9	7.3	7.8
20	25–102	48.000–202.000	154	29.5	12.5	373.5	78.3	76.3	11.2	20.1	520.8	160.8	12.3	12.9
21	25–102	48.000–202.000	154	27.5	12.9	357.8	76.1	77.1	10.8	17.9	553.8	193.8	17.8	18.9
23	52–102	102.000–202.000	100	25.5	13.1	337.1	70.8	83.9	10.5	14.1	503.6	143.6	14.9	17.0
26	74–102	146.000–202.000	56	152.7	26.3	4017.7	395.0	32.4	44.0	51.1	1599.7	1239.7	5.2	6.1
			MEAN	41.6	15.7	763.3	114.5	71.8	15.0	21.2	677.7	318.4	13.6	15.5
			±S.D.	29.7	4.4	861.5	77.4	14.9	8.1	8.8	284.3	284.7	4.3	5.0

4. Stacked perimeter plots (Figs. 3e, 4c and 5a) are another means of displaying dynamic cell shapes over time and are useful in evaluating the frequency of lateral pseudopod extension and directional persistence, especially in the comparison of mutant or defective cells with their normal counterparts (Figs. 4d and 5b) [10, 65, 66].
5. Cytoskeletal defects can often be detected in measurements of membrane protrusions [24, 36]. This information can be visualized quickly and effectively on large numbers of cells through the use of "difference pictures" [60, 61, 63] (Fig. 4a). Difference pictures are constructed by overlaying the outline of the cell at frame *n-x* with the outline of the current frame *n* where *x* is the user-specified interval. Expansion zones are regions into which the cell expanded during the specified interval (black areas in Fig. 4a) and retraction zones are regions from which the cell retracted (hatched areas in Fig. 4a). Areas shared in the two images are color-coded gray.
6. The area contained within expansion and retraction zones as determined from differencing can be quantified in J3D-DIAS4.1. This measurement can be used to determine if cytoskeletal mutants are defective in force generation required to extend lamellipodia or pseudopod or to retract the uropod [67–69]. The user windows the localized expansion or retraction zone from a series of difference pictures (Fig. 4a). The percent of the total area within the window is then calculated.

3.6 Sample Preparation for 3D Analysis of 3D Culture

1. Modify the Petri dish for use with DIC optics and to fit within the allowable working distance of the microscope (*see* **Notes 6** and 7).
2. Using a sterile, pre-chilled pipet tip, apply 100 μL of ice cold Matrigel onto the 30 mm glass insert of a pre-chilled 65 mm Petri dish, taking care not to introduce bubbles.
3. Incubate the Petri dish for 30 min at 37 °C.

Fig. 4 (continued) (*black*) and retraction zones (*hatched*) can be visualized in difference pictures. Relative flow is measured from a difference picture by windowing the area of interest (*boxes*) at 0, 4, and 14 min. The percent of the total area contained within the window is calculated and displayed alongside the window. (*b*) Unwrapping and stacking the cell perimeter over time provides a history of expansions and can be used to detect cyclical shape changes. (*c*) Comparison of stacked perimeter plots of control, *ptenA*$^-$, *lpten*$^-$, and *ptenA*$^-$ cells overexpressing *lpten* (*ptenA*$^-$/*lpten*^{oe}) in the model system *D. discoideum* reveal significant defects in instantaneous velocity in *ptenA*$^-$ cells and increased lateral pseudopod extension in *lpten*$^-$ cells [43]. The final shape in the time series of the stacked perimeter plots is shaded *dark gray*. Interestingly, overexpression of *lpten* in *ptenA*$^-$ background rescues the velocity and shape defects in *ptenA*$^-$, conclusions confirmed by quantitative parameters (*d*). (*e*) 3D reconstructions of control and *lpten*$^-$ cells migrating on a 2D substrate reveal that the majority of lateral pseudopods extended by *lpten*$^-$ cells (*arrows*) are off the surface and therefore do not produce turns [71]

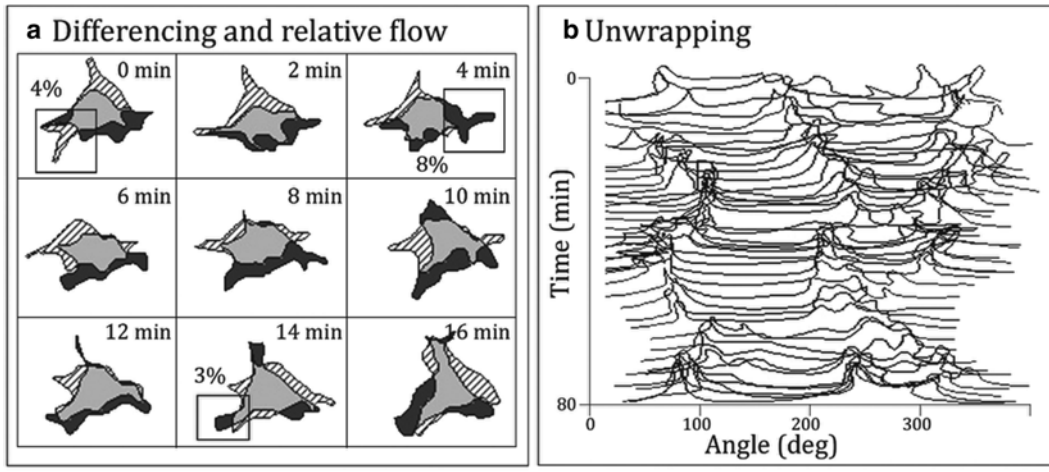

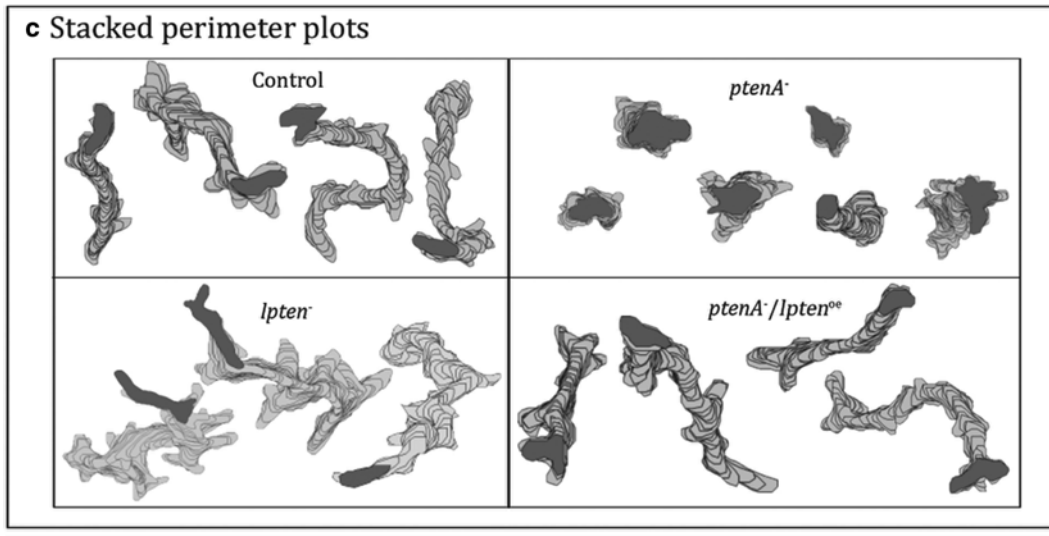

d Sample parameters

Cell type	Inst. Vel. (μm /min)	Percent cells ≥ 9 μm/min	Percent motile cells	Lateral pseudopods per 10 min
Control	8.3 ± 3.6	43%	83%	5.3 ± 1.5
ptenA$^-$	3.6 ± 0.7	0%	21%	9.5 ± 2.2
lpten$^-$	7.7 ± 2.7	25%	98%	12.4 ± 2.9
ptenA$^-$ /*lpten*^{oe}	7.5 ± 2.1	21%	90%	5.8 ± 1.7

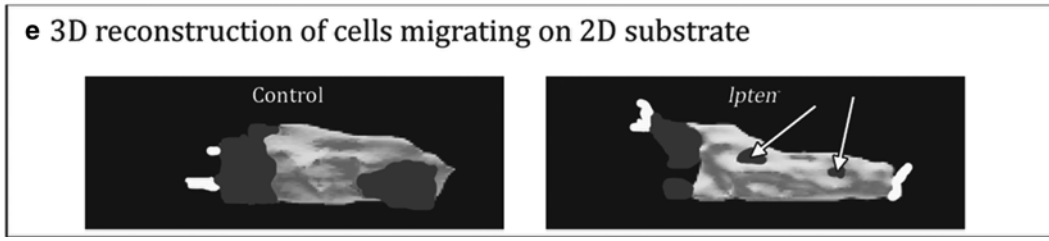

Fig. 4 2D cell shape parameters available in J3D-DIAS4.1 provide dynamical information. (*a*) Difference pictures at 2 min intervals of a cell from a human cancer cell line migrating on a 2D Matrigel substrate. Expansion zones

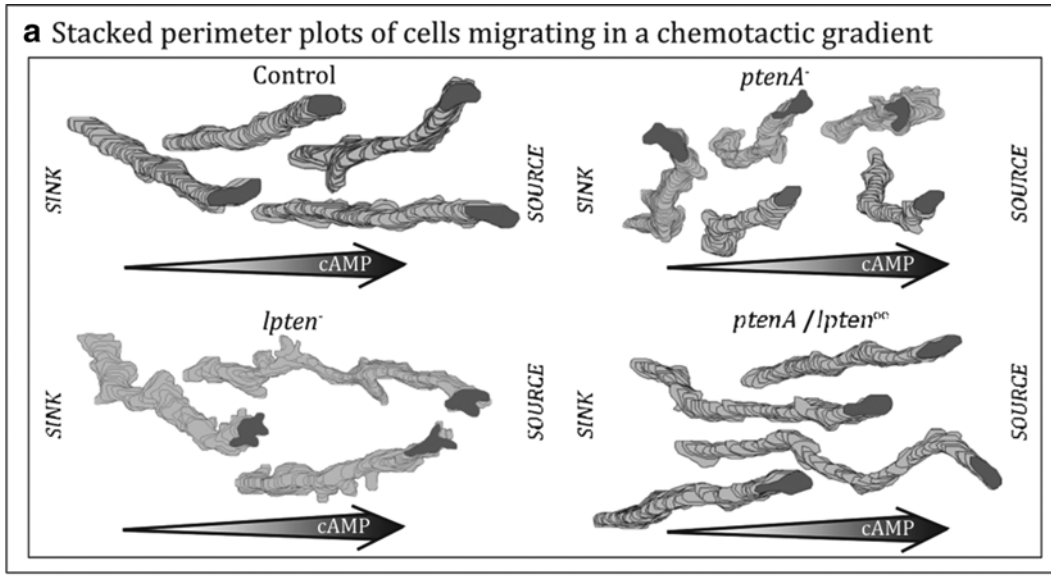

b Motion analysis parameters

Cell type	Inst. Vel. (μm /min)	Percent cells ≥ 9 μm/min	Chem. Index (C.I.)	Percent Positive C.I.	Percent motile cells	Lateral pseudopods per 10 min
Control	9.0 ± 4.0	41%	+0.56 ± 0.22	100%	93%	1.0 ± 0.7
ptenA$^-$	5.3 ± 1.5	0%	+0.18 ± 0.26	80%	72%	3.8 ± 1.7
lpten$^-$	9.8 ± 3.0	51%	+0.63 ± 0.33	99%	100%	5.2 ± 1.4
ptenA$^-$ /*lpten*^{oe}	7.6 ± 2.4	27%	+0.66 ± 0.16	100%	96%	1.1 ± 0.6

Fig. 5 Comparison of 2D cell shape and motion parameters in control, *ptenA*$^-$, *lpten*$^-$, and *ptenA*$^-$/*lpten*^{oe} strains in *D. discoideum* demonstrates that cells from all strains, with the exception of *ptenA*$^-$, are capable of efficient chemotaxis. (*a*) Stacked perimeter plots of control, *ptenA*$^-$, *lpten*$^-$, and *ptenA*$^-$/*lpten*^{oe} migrating in a Zigmond chamber in the presence of a spatial gradient of cAMP. The source of the gradient is to the *right*, as indicated by the direction of the *large arrow* at the *bottom* of *each panel*. The final shape in the time series of the stacked perimeter plots is shaded *dark gray*. (*b*) Sample motion analysis parameters computed by J3D-DIAS4.1 demonstrate that *ptenA*$^-$ defects in velocity and later pseudopod suppression in a spatial gradient of cAMP are rescued by over-expression of *lpten* in *ptenA*$^-$ background

4. Dissociate cells from tissue culture flask, resuspend in media, wash, resuspend in fresh media, and count.
5. Withdraw the volume required to yield 5×10^5 cells, bring the total volume up to 250 μL and chill.
6. Add 500 μL of ice cold Matrigel to the 100 μL of chilled cell suspension and mix by gently pipetting up and down. Distribute the entire 750 μL onto the Matrigel-coated cover slip (*see* Fig. 2a).

7. Incubate for 30 min to allow gelation.
8. Add 2–3 mL of media to the dish.
9. Place preparation on the stage of the 3D microscope and begin image acquisition (Fig. 2b).

3.7 Optical Sectioning

1. For 3D analysis of basic motile behavior on a 2D substrate, samples are inoculated into a perfusion chamber. The chamber is connected to a perfusion pump and positioned on the stage of an inverted microscope equipped with DIC optics and a high numerical aperture objective such as the Zeiss 63× Planapochromat.
2. To obtain optical sections of single cells such as *D. discoideum* amoebae or human PMNs migrating on a 2D substrate, program the motor to move through the *z*-axis height, generally 10–20 μm, in 2–3 s and repeat the process every 4–5 s for 5–10 min per cell (Fig. 4e) (*see* **Note 17**).
3. For 3D analysis of cells embedded in a 3D matrix, place the 3D culture on the stage of a microscope with environmental controls or contained within a 5 % CO_2, 37 °C incubator. Set the top and bottom of the z range, the z increment, the time interval between acquisition of each z-series, and the length of the experiment as shown in Fig. 2c (*see* **Note 18**).
4. The acquisition software typically generates a numbered JPEG image stack that can be played and saved as a movie (Fig. 2c). Objects are then detected from this movie as described below.

3.8 Object Detection and Reconstruction in 4D Experiment

1. Bitmapping is a rapid and accurate method to detect objects (Fig. 6a). This method distinguishes a cell or group of cells based on the fact that they exhibit a higher grayscale variation than the background. More specifically, bitmapping assigns a 0–256 gray scale value to individual pixels within a user-defined kernel; i.e., a 3×3, 5×5 or 7×7 pixel matrix. The gray scale values within the kernel are averaged, the standard deviation (sd) computed and that sd is assigned to a reference pixel within the kernel. If the referenced sd is above the user-determined threshold value, then the pixel is considered part of the object and is retained as such. The kernel moves by one pixel and the process is repeated until every pixel within the field is scanned. Background or out of focus objects in each optical section will have more uniform gray scale values, lower sd values and thus be discarded. One advantage of bitmap tracing over outlining is that holes, gaps or concave indentations present within the real image are maintained.
2. Manual outlining can be used for single cells and fine structures such as filopodia (Fig. 6b).

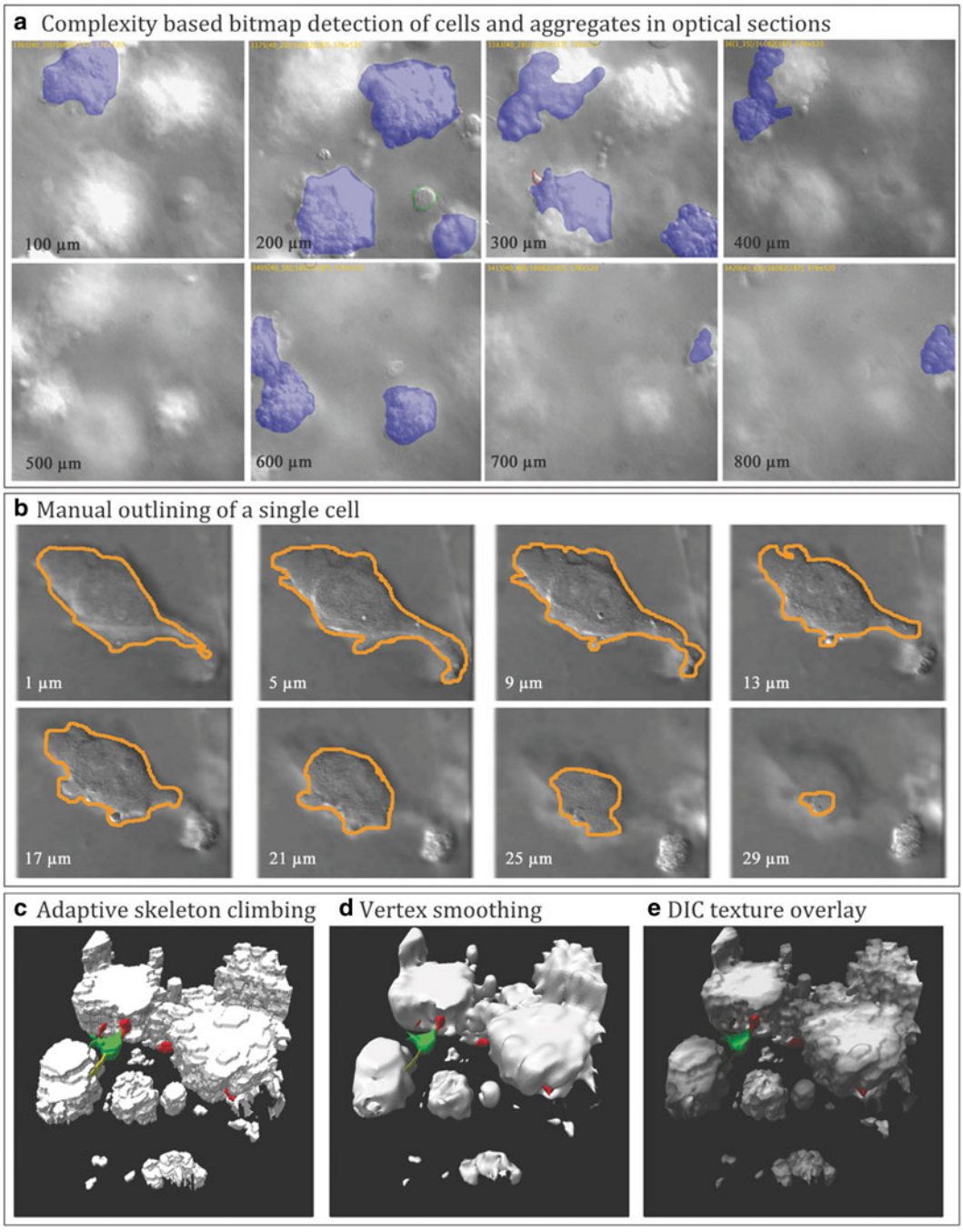

Fig. 6 Examples of automatic bitmap object detection, manual outlining of single cells, and 3D reconstruction methods. (*a*) Fields of cells and aggregates within a 3D matrix optically sectioned at 30-min intervals for 30 days generates movies comprised of over 100,000 frames. Cells and aggregates can be identified in these movies by complexity based automatic bitmap detection. (*b*) Single cells and organelles can be manually traced in optical sections. (*c*–*e*) Methods for 3D reconstructions combining automatically detected and manually detected objects. Coalescing aggregates in preparations of cancer cells are color-coded gray, facilitator cell and filopodia are color-coded *green* and *yellow*, respectively, and probe cells, *red*

3. Overlapping traces are stacked into a 3D z-series, either as a complexity stack in the case of bitmap tracings or as a series of beta-spline replacements (*see* **Note 19**), in the case of outlines.
4. Outlines are filled with voxels (3D pixels) and bitmap pixels are expanded into voxels. In both cases, the *x*, *y*, and *z* scales determine the voxel dimensions.
5. Java OpenGL (JOGL) implemented in J3D-DIAS4.1 performs 4D reconstructions using the "adaptive skeleton climbing isoform extraction" method [70], a variation of the "marching cubes" algorithm (Fig. 6c; *see* **Note 20**).
6. Vertices are smoothed three times to attenuate the sharp edges in the surface of the object (Fig. 6d) (*see* **Note 21**). DIC texture overlay can be added to restore details present in the original image (Fig. 6e).
7. Manually and automatically traced cells can be combined into a single movie file, reconstructed as wireframe images or as solid, shaded nontransparent objects, such as the cells shown in Fig. 6d, e. Filopodia, lamellipodia, and nuclei or other organelles can be independently color-coded.
8. Images can be rotated and viewed from different angles and saved as a movie.
9. Mechanisms of coalescence and the presence of different cell types can be analyzed in 4D in preparations of cancer cells. In Fig. 6c a facilitator cell (color-coded green) that emerged from an aggregate of a tumorigenic cell line contacted a probe cell (color-coded red) that emerged from another aggregate. The facilitator and probe then pulled the two aggregates together, resulting in coalescence.
10. The effects of potential anticancer therapies including monoclonal antibodies can be evaluated in 4D as shown in Fig. 7.

3.9 4D Motility and Dynamic Morphology Parameters

1. The 3D cell center (3D centroid) can be determined by averaging the *x*-, *y*-, and *z*-coordinates of the interior points of the faceted object and used to generate 4D paths.
2. Instantaneous velocity is calculated from the 3D position of the centroid by the central difference method [62] using the 2D formulae described earlier [60] (*see* **Note 14**). Other 2D parameters calculated from the centroid position can likewise be extrapolated to 3D.
3. The triangularized faceted surface is a polyhedron. *See*http://wwwf.imperial.ac.uk/~rn/centroid.pdf to find the standard calculus formulae to determine the volume of a polyhedron.
4. The "surface complexity" function was introduced into J3D-DIAS4.1 as a means to quantify the activity around the periph-

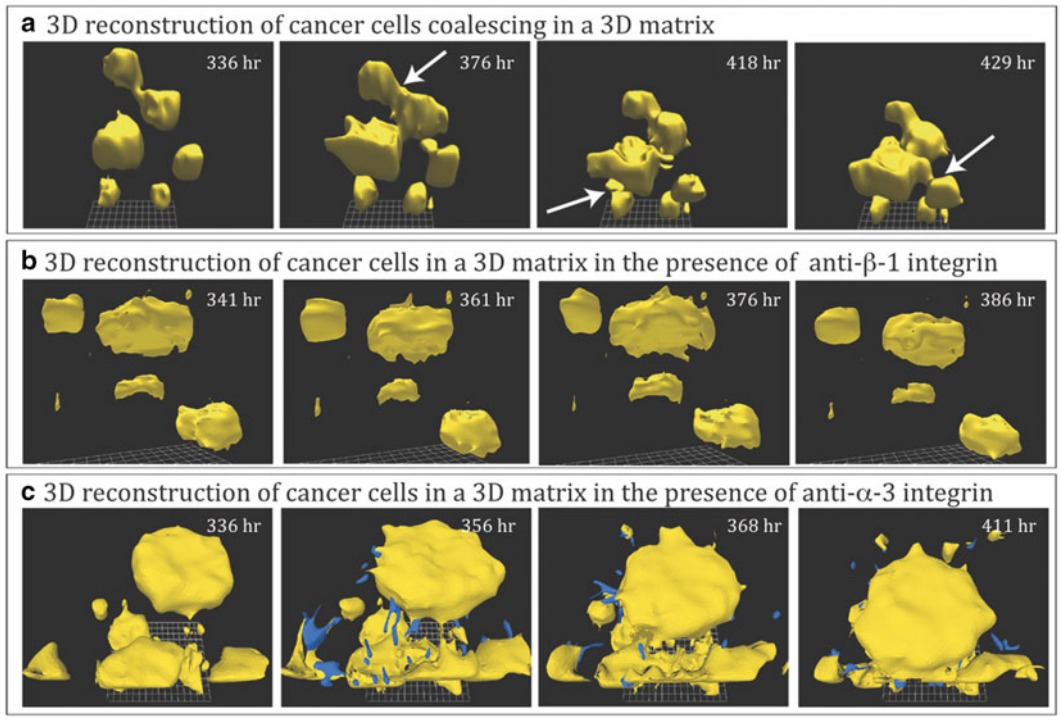

Fig. 7 J3D-DIAS4.1 generated 3D reconstructions of cancer cells and aggregates embedded in a 3D Matrigel matrix reveal effects of potential anticancer treatments such as monoclonal antibodies on cell growth, coalescence and single cell behavior. (*a*) Untreated cancer cells coalesce into aggregates in a 3D matrix as indicated by the *white arrows*. (*b*) Aggregate coalescence is inhibited in identical cultures treated with anti-β-1 integrin monoclonal antibody (AIIB2). (*c*) Aggregate coalescence and rapid exit of single cells from the aggregates (color-coded *blue*) are stimulated in identical cultures treated with anti-α-3 integrin monoclonal antibody (P1B5), demonstrating that differential effects of different treatments are detected in the 4D analysis

ery of aggregates formed in cancer cell cultures (Scherer et al. submitted). The surface complexity parameter is the reciprocal of 3D roundness (*see* **Note 22**).

4 Notes

1. To insure that experiments are performed on exponentially dividing populations of cells and to minimize accumulation of spontaneous mutations, *D. discoideum* cells should be routinely passaged before reaching stationary phase (~1×10^7 cells/mL). In addition, fresh cultures should be reconstituted from frozen stocks every 4–6 weeks.
2. Protocols can be found at the web site for the Center for Disease Control http://www.cdc.gov/biosafety/publications/bmbl5/index.htm and/or through the Research Office at the institution where the work is being performed. All human tissues

and/or blood products must be obtained under informed consent using protocols approved by the institution's IRB.

3. Heat inactivation of serum is no longer recommended for most cell culture applications (http://www.sigmaaldrich.com/technical-documents/protocols/biology/the-cell-environment.html).
4. Matrigel matrix will gel quickly, so care must be taken during preparation to keep it, as well as the surfaces and media that it contacts, chilled.
5. If the height of the dish exceeds the working distance of the optics, then approximately 5 mm can be trimmed from the dish bottom with sterile scissors before media is added.
6. For optical sectioning using DIC, a glass window should replace the plastic in the light path through the lid of the dish. An area with a diameter of 20–30 mm can be removed from the center of the plastic lid with a drill bit or laser cutter. A glass cover slip of larger dimensions can then be placed over the hole and sealed with Vaseline. The lid with the glass window is sterilized with ethanol and/or UV exposure within the biosafety cabinet.
7. J3D-DIAS4.1 can be accessed by collaboration at the W.M. Keck Dynamic Image Analysis Facility, David R. Soll, director, Biology Department, University of Iowa, Iowa City, IA 52245 USA.
8. The z-height is empirically determined and depends on the cells being studied. The acquisition time for an individual z-series and the interval between each z-series can be increased for slower moving cells.
9. LED light significantly reduces phototoxicity during long-term imaging but is generally not necessary for *D. discoideum* and PMNs.
10. Inoculation of a dilute cell suspension along with continual perfusion prevents accumulation of cAMP in the chamber, thereby eliminating its effects on cell behavior.
11. Pre-fill syringe, inlet tube, and needle with appropriate solution so as to avoid air bubbles.
12. Image processing algorithms such as differencing, black filtering and white filtering can facilitate automatic edge detection, particularly in images with a "phase halo." Differencing copies the image, shifts the copy by one pixel in the horizontal direction, one pixel in the vertical direction, and then subtracts the two images. Neutral gray (128) is added to the resulting intensities. To black filter, pixels darker than a user determined threshold are detected and removed from a bitmap outline. Conversely, to white filter, pixels lighter than user-determined threshold are detected and removed from the bitmap outline.

13. The initial outline is a connected circuit of pixels determine by the threshold setting. Beta splines replace the outline with curves approximating the original pixels. Because the original pixel outline is likely to be jagged, "spline resolution" functions can be applied. These functions remove some of the pixels, allowing the calculation of splines and generation of a smooth, rather than stair-stepped, final outline. Bias and tension functions also can be applied to adjust the accuracy of the final outline.
14. The speed of cellular translocation (instantaneous velocity) is calculated by the central difference method [62] as follows [60]:

    Speed[f] = (**scale** x **frate**)x **sqrt**(((**x**[f+**I**]-**x**[f-**I**])/2**I**)^2 + ((**y**[f+**I**]-**y**[f-**I**])/2**I**)^2 + ((**z**f+**I**]-**z**[f-**I**])/2**I**)^2))) when 1 <= f-**I** and f+**I** <=**F**

    Speed[f] = (**scale** x **frate**)x **sqrt**(((**x**[f+**I**]-**x**[f])/**I**)^2 + ((**y**[f+**I**]-**y**[f])/**I**)^2 + ((**z**f+**I**]-**z**[f-I])/2**I**)^2))) when f-**I** < 1 and f+**I** <= **F** (first frame)

    Speed [f] = (**scale** x **frate**)x **sqrt**(((**x**[f]-**x**[f-**I**])/**I**)^2 + ((**y**[f]-**y**[f-**I**])/**I**)^2 + ((**z**f+**I**]-**z**[f-I])/2**I**)^2))) when 1 <=f-**I** and f+**I** > **F** (last frame),

    where **F** is the total number of frames,

    f is the "current" frame,

    (**x**[f],**y**[f]) are the coordinates of the centroid of an object in frame f, 1 <=f<=**F**,

    I is the centroid increment,

    frate is the frame rate in # of frames per unit time,

    scale is the scale factor in distance units per pixel,

    sqrt is the square root function, and

    x denotes multiplication.

    Speed [f] = 0
15. Direction of travel using the central difference method is calculated as follows:

    Dir[f] = **angle**((**x**[f+**I**]-**x**[f-**I**]), (**y**[f+**I**]-**y**[f-**I**]))

    when 1 <=f-**I** and f+**I** <=**F**

    Dir[f] = **angle**((**x**[f+**I**]-**x**[f]), (**y**[f+**I**]-**y**[f])) when f-**I** < 1 and f+**I** <=**F**

    Dir[f] = **angle**((**x**[f]-**x**[f-**I**]), (**y**[f]-**y**[f-**I**])) when 1 <=f-**I** and f+**I** > **F**

    Dir[f] = 0 otherwise

    Multiples of ±360° are added to the direction to make the graph continuous.
16. Direction change using the central difference method is calculated as follows:

DirCh[f] = 0 when f-**I** < 1 **DirCh**[f] = **abs**(**Dir**[f]-**Dir**[f-**I**]) otherwise

If the direction change is greater than 180°, it is subtracted from 360. This always gives values between 0 and 180°

17. 3D movies of single cells migrating on a 2D substrate are typically comprised of 30–60 optical sections per individual z-series. The height is due to the fact that these cells often lift the anterior off the substrate and can extend pseudopodia in the *z* plane [71–73]. Ten minutes of optical sectioning, therefore, will generate a movie that is 3600–7200 individual frames.
18. We typically optically section cells and cell aggregates through 1 mm of Matrigel at 5–10 μm increments every 30 min over a period of 14–30 days or longer if media is refreshed. This process can therefore yield 122,000 optical sections per preparation per period of analysis.
19. Beta-splines replace the pixels in the outline with curves that approximate the original pixels [58]. In essence, beta-splines smooth the outline by applying bias, tension, and resolution [60] and generate a mathematical model from which data can then be calculated [59, 60, 63, 74].
20. Descriptively, in adaptive skeleton climbing a triangular facet is assigned to the raw voxel block in the most stable possible configuration. The user determines the size of the facet; the smaller the size, the greater the complexity of the surface. The remaining facets are then placed in the most stable possible configuration. Finally, irregularly shaped facets are added to any spaces between facets.
21. The *x*, *y*, and *z* coordinates of each vertex are averaged with neighboring *x*, *y*, and *z* coordinates [75].
22. 1/(6x **sqrt** xVol/(surface area$^{3/2}$)) where sqrt is the square root, Vol is the volume and surface area is the sum of the area of all facets. This yields a value for surface complexity that increases, rather than decreases, with increasing complexity.

Acknowledgments

This work was supported by the Developmental Studies Hybridoma Bank (DSHB), a National Resource created by the NICHD of the NIH and maintained at The University of Iowa, Department of Biology, Iowa City, IA 52242. We thank Brett Hanson, Joseph Ambrose, Kanoe Russell, Emma Buchele, Brian Kroll, Michele Livitz, Benjamin Soll, and Nicole Richardson for technical assistance. The monoclonal antibodies AIIB2, developed by C.H. Damsky, and P1B5, developed by E.A. Wayner and W.G. Carter, were obtained from the DSHB.

References

1. Wang MJ, Artemenko Y, Cai WJ, Iglesias PA, Devreotes PN (2014) The directional response of chemotactic cells depends on a balance between cytoskeletal architecture and the external gradient. Cell Rep 9:1110–1121
2. Danuser G, Allard J, Mogilner A (2013) Mathematical modeling of eukaryotic cell migration: insights beyond experiments. Annu Rev Cell Dev Biol 29:501–528
3. Doyle AD, Petrie RJ, Kutys ML, Yamada KM (2013) Dimensions in cell migration. Curr Opin Cell Biol 25:642–649
4. Ridley AJ, Schwartz MA, Burridge K, Firtel RA, Ginsberg MH, Borisy G, Parsons JT, Horwitz AR (2003) Cell migration: integrating signals from front to back. Science 302:1704–1709
5. Biname F, Pawlak G, Roux P, Hibner U (2010) What makes cells move: requirements and obstacles for spontaneous cell motility. Mol Biosyst 6:648–661
6. Annesley SJ, Fisher PR (2009) Dictyostelium discoideum--a model for many reasons. Mol Cell Biochem 329:73–91
7. Alvarez-Gonzalez B, Meili R, Firtel R, Bastounis E, Del Alamo JC, Lasheras JC (2014) Cytoskeletal mechanics regulating amoeboid cell locomotion. Appl Mech Rev 66:pii: 050804
8. Davidson AJ, Insall RH (2013) SCAR/WAVE: a complex issue. Commun Integr Biol 6:e27033
9. Soll DR, Wessels D, Kuhl S, Lusche DF (2009) How a cell crawls and the role of cortical myosin II. Eukaryot Cell 8:1381–1396
10. Wessels D, Lusche DF, Scherer A, Kuhl S, Myre MA, Soll DR (2014) Huntingtin regulates Ca(2+) chemotaxis and K(+)-facilitated cAMP chemotaxis, in conjunction with the monovalent cation/H(+) exchanger Nhe1, in a model developmental system: insights into its possible role in Huntingtons disease. Dev Biol 394:24–38
11. Futosi K, Fodor S, Mocsai A (2013) Neutrophil cell surface receptors and their intracellular signal transduction pathways. Int Immunopharmacol 17:638–650
12. Kumar S, Xu J, Kumar RS, Lakshmikanthan S, Kapur R, Kofron M, Chrzanowska-Wodnicka M, Filippi MD (2014) The small GTPase Rap1b negatively regulates neutrophil chemotaxis and transcellular diapedesis by inhibiting Akt activation. J Exp Med 211:1741–1758
13. Itakura A, Aslan JE, Kusanto BT, Phillips KG, Porter JE, Newton PK, Nan X, Insall RH, Chernoff J, McCarty OJ (2013) p21-Activated kinase (PAK) regulates cytoskeletal reorganization and directional migration in human neutrophils. PLoS One 8:e73063
14. Niggli V (2003) Signaling to migration in neutrophils: importance of localized pathways. Int J Biochem Cell Biol 35:1619–1638
15. Rougerie P, Miskolci V, Cox D (2013) Generation of membrane structures during phagocytosis and chemotaxis of macrophages: role and regulation of the actin cytoskeleton. Immunol Rev 256:222–239
16. Pixley FJ (2012) Macrophage migration and its regulation by CSF-1. Int J Cell Biol 2012: 501962
17. Geiger TR, Peeper DS (2009) Metastasis mechanisms. Biochim Biophys Acta 1796: 293–308
18. Yilmaz M, Christofori G, Lehembre F (2007) Distinct mechanisms of tumor invasion and metastasis. Trends Mol Med 13:535–541
19. Safdari Y, Khalili M, Ebrahimzadeh MA, Yazdani Y, Farajnia S (2015) Natural inhibitors of PI3K/AKT signaling in breast cancer: emphasis on newly-discovered molecular mechanisms of action. Pharmacol Res 93:1
20. Castillo-Pichardo L, Humphries-Bickley T, De La Parra C, Forestier-Roman I, Martinez-Ferrer M, Hernandez E, Vlaar C, Ferrer-Acosta Y, Washington AV, Cubano LA et al (2014) The rac inhibitor EHop-016 inhibits mammary tumor growth and metastasis in a nude mouse model. Transl Oncol 7:546–555
21. Nguyen DX, Bos PD, Massague J (2009) Metastasis: from dissemination to organ-specific colonization. Nat Rev Cancer 9:274–284
22. Fidler IJ (2002) Critical determinants of metastasis. Semin Cancer Biol 12:89–96
23. Eccles SA, Welch DR (2007) Metastasis: recent discoveries and novel treatment strategies. Lancet 369:1742–1757
24. Ishihara D, Dovas A, Park H, Isaac BM, Cox D (2012) The chemotactic defect in wiskott-Aldrich syndrome macrophages is due to the reduced persistence of directional protrusions. PLoS One 7:e30033
25. Soll DR, Wessels D, Heid PJ, Zhang H (2002) A contextual framework for characterizing motility and chemotaxis mutants in Dictyostelium discoideum. J Muscle Res Cell Motil 23:659–672
26. Hind LE, Mackay JL, Cox D, Hammer DA (2014) Two-dimensional motility of a macrophage cell line on microcontact-printed fibronectin. Cytoskeleton 71:542–554

27. Charras G, Sahai E (2014) Physical influences of the extracellular environment on cell migration. Nat Rev Mol Cell Biol 15:813–824
28. Chang Stephanie S, Guo W-h, Kim Y, Wang Y-l (2013) Guidance of cell migration by substrate dimension. Biophys J 104:313–321
29. Corall S, Haraszti T, Bartoschik T, Spatz J, Ludwig T, Cavalcanti-Adam E (2014) \upalpha 5\upbeta 1-integrin and MT1-MMP promote tumor cell migration in 2D but not in 3D fibronectin microenvironments. Comput Mech 53:499–510
30. Page-McCaw A, Ewald AJ, Werb Z (2007) Matrix metalloproteinases and the regulation of tissue remodelling. Nat Rev Mol Cell Biol 8:221–233
31. Stepanovic V, Wessels D, Goldman FD, Geiger J, Soll DR (2004) The chemotaxis defect of Shwachman-Diamond Syndrome leukocytes. Cell Motil Cytoskeleton 57:158–174
32. Williams RS, Boeckeler K, Graf R, Muller-Taubenberger A, Li Z, Isberg RR, Wessels D, Soll DR, Alexander H, Alexander S (2006) Towards a molecular understanding of human diseases using Dictyostelium discoideum. Trends Mol Med 12:415–424
33. Van Goethem E, Poincloux R, Gauffre F, Maridonneau-Parini I, Le Cabec V (2010) Matrix architecture dictates three-dimensional migration modes of human macrophages: differential involvement of proteases and podosome-like structures. J Immunol 184:1049–1061
34. Roh-Johnson M, Bravo-Cordero JJ, Patsialou A, Sharma VP, Guo P, Liu H, Hodgson L, Condeelis J (2014) Macrophage contact induces RhoA GTPase signaling to trigger tumor cell intravasation. Oncogene 33:4203–4212
35. Zhang Y, Choksi S, Chen K, Pobezinskaya Y, Linnoila I, Liu Z-G (2013) ROS play a critical role in the differentiation of alternatively activated macrophages and the occurrence of tumor-associated macrophages. Cell Res 23:898–914
36. Sidani M, Wessels D, Mouneimne G, Ghosh M, Goswami S, Sarmiento C, Wang W, Kuhl S, El-Sibai M, Backer JM (2007) Cofilin determines the migration behavior and turning frequency of metastatic cancer cells. J Cell Biol 179:777–791
37. Starke J, Maaser K, Wehrle-Haller B, Friedl P (2013) Mechanotransduction of mesenchymal melanoma cell invasion into 3D collagen lattices: filopod-mediated extension–relaxation cycles and force anisotropy. Exp Cell Res 319:2424–2433
38. Wang Y, McNiven MA (2012) Invasive matrix degradation at focal adhesions occurs via protease recruitment by a FAK-p130Cas complex. J Cell Biol 196:375–385
39. Gligorijevic B, Bergman A, Condeelis J (2014) Multiparametric classification links tumor microenvironments with tumor cell phenotype. PLoS Biol 12:e1001995
40. Murphy DA, Courtneidge SA (2011) The 'ins' and 'outs' of podosomes and invadopodia: characteristics, formation and function. Nat Rev Mol Cell Biol 12:413–426
41. Linder S, Wiesner C (2015) Tools of the trade: podosomes as multipurpose organelles of monocytic cells. Cell Mol Life Sci 72:121
42. Heid PJ, Geiger J, Wessels D, Voss E, Soll DR (2005) Computer-assisted analysis of filopod formation and the role of myosin II heavy chain phosphorylation in Dictyostelium. J Cell Sci 118:2225–2237
43. Lusche DF, Wessels D, Richardson NA, Russell KB, Hanson BM, Soll BA, Lin BH, Soll DR (2014) *PTEN* redundancy: overexpressing *lpten*, a homolog of *Dictyostelium discoideum ptenA*, the ortholog of human *PTEN*, rescues all behavioral defects of the mutant ptenA-. PLoS One 9:e108495
44. Volk AP, Heise CK, Hougen JL, Artman CM, Volk KA, Wessels D, Soll DR, Nauseef WM, Lamb FS, Moreland JG (2008) ClC-3 and IClswell are required for normal neutrophil chemotaxis and shape change. J Biol Chem 283:34315–34326
45. Scherer A, Kuhl S, Wessels D, Lusche DF, Hanson B, Ambrose J, Voss E, Fletcher E, Goldman C. and Soll DR (2015) A Computer-Assisted 3D Model for Analyzing the Aggregation of Tumorigenic Cells Reveals Specialized Behaviors and Unique Cell Types that Facilitate Aggregate Coalescence. PLoS ONE. 10.1371/journal.pone.0118628
46. Soll DR, Wessels D, Heid PJ, Voss E (2003) Computer-assisted reconstruction and motion analysis of the three-dimensional cell. ScientificWorldJournal 3:827–841
47. Varnum B, Edwards KB, Soll DR (1985) Dictyostelium amebae alter motility differently in response to increasing versus decreasing temporal gradients of cAMP. J Cell Biol 101:1–5
48. Wessels D, Brincks R, Kuhl S, Stepanovic V, Daniels KJ, Weeks G, Lim CJ, Spiegelman G, Fuller D, Iranfar N et al (2004) RasC plays a role in transduction of temporal gradient information in the cyclic-AMP wave of Dictyostelium discoideum. Eukaryot Cell 3:646–662
49. Geiger J, Wessels D, Soll DR (2003) Human polymorphonuclear leukocytes respond to waves of chemoattractant, like Dictyostelium. Cell Motil Cytoskeleton 56:27–44

50. Heid PJ, Wessels D, Daniels KJ, Gibson DP, Zhang H, Voss E, Soll DR (2004) The role of myosin heavy chain phosphorylation in Dictyostelium motility, chemotaxis and F-actin localization. J Cell Sci 117:4819–4835
51. Shutt DC, Jenkins LM, Carolan EJ, Stapleton J, Daniels KJ, Kennedy RC, Soll DR (1998) T cell syncytia induced by HIV release. T cell chemoattractants: demonstration with a newly developed single cell chemotaxis chamber. J Cell Sci 111(Pt 1):99–109
52. Lusche DF, Wessels D, Scherer A, Daniels K, Kuhl S, Soll DR (2012) The IplA Ca2+ channel of Dictyostelium discoideum is necessary for chemotaxis mediated through Ca2+, but not through cAMP, and has a fundamental role in natural aggregation. J Cell Sci 125: 1770–1783
53. Scherer A, Kuhl S, Wessels D, Lusche DF, Raisley B, Soll DR (2010) Ca2+ chemotaxis in Dictyostelium discoideum. J Cell Sci 123:3756–3767
54. Skoge M, Adler M, Groisman A, Levine H, Loomis WF, Rappel WJ (2010) Gradient sensing in defined chemotactic fields. Integr Biol (Camb) 2:659–668
55. Varnum B, Edwards KB, Soll DR (1986) The developmental regulation of single-cell motility in Dictyostelium discoideum. Dev Biol 113:218–227
56. Varnum B, Soll DR (1981) Chemoresponsiveness to cAMP and folic acid during growth, development, and dedifferentiation in Dictyostelium discoideum. Differentiation 18:151–160
57. Hoeller O, Kay RR (2007) Chemotaxis in the absence of PIP3 gradients. Curr Biol 17:813–817
58. Barsky B (1988) Computer graphics and geometric modeling using beta-splines. Springer, New York, NY
59. Soll D, Voss E (1998) Two and three dimensional computer systems for analyzing how cells crawl. In: Soll D, Wessels D (eds) Motion analysis of living cells. John Wiley, Inc., New York, NY, pp 25–52
60. Soll DR (1995) The use of computers in understanding how animal cells crawl. Int Rev Cytol 163:43–104
61. Soll DR, Wessels D, Voss E, Johnson O (2001) Computer-assisted systems for the analysis of amoeboid cell motility. Methods Mol Biol 161:45–58
62. Maron MJ (1982) Numerical analysis. Macmillan, New York, NY
63. Soll DR, Voss E, Johnson O, Wessels D (2000) Three-dimensional reconstruction and motion analysis of living, crawling cells. Scanning 22:249–257
64. Soll DR, Voss E, Varnum-Finney B, Wessels D (1988) "Dynamic Morphology System": a method for quantitating changes in shape, pseudopod formation, and motion in normal and mutant amoebae of Dictyostelium discoideum. J Cell Biochem 37:177–192
65. Chung CY, Lee S, Briscoe C, Ellsworth C, Firtel RA (2000) Role of Rac in controlling the actin cytoskeleton and chemotaxis in motile cells. Proc Natl Acad Sci 97:5225–5230
66. Wessels D, Lusche DF, Steimle PA, Scherer A, Kuhl S, Wood K, Hanson B, Egelhoff TT, Soll DR (2012) Myosin heavy chain kinases play essential roles in Ca2+, but not cAMP, chemotaxis and the natural aggregation of Dictyostelium discoideum. J Cell Sci 125:4934–4944
67. Wessels D, Murray J, Jung G, Hammer JA 3rd, Soll DR (1991) Myosin IB null mutants of Dictyostelium exhibit abnormalities in motility. Cell Motil Cytoskeleton 20:301–315
68. Soll D, Wessels D (1998) Computer-assisted characterization of the behavioral defects of cytoskeletal mutants of Dictyostelium discoideum. In: Soll D, Wessels D (eds) Motion analysis of living cells. John Wiley, Inc., New York, NY, pp 101–140
69. Wessels D, Soll DR, Knecht D, Loomis WF, De Lozanne A, Spudich J (1988) Cell motility and chemotaxis in Dictyostelium amebae lacking myosin heavy chain. Dev Biol 128:164–177
70. Poston T, Wong TT, Heng PA (1998) Multiresolution isosurface extraction with adaptive skeleton climbing. Comput Graph Forum 17:137
71. Wessels D, Reynolds J, Johnson O, Voss E, Burns R, Daniels K, Garrard E, O'Halloran TJ, Soll DR (2000) Clathrin plays a novel role in the regulation of cell polarity, pseudopod formation, uropod stability and motility in Dictyostelium. J Cell Sci 113(Pt 1):21–36
72. Wessels D, Vawter-Hugart H, Murray J, Soll DR (1994) Three-dimensional dynamics of pseudopod formation and the regulation of turning during the motility cycle of Dictyostelium. Cell Motil Cytoskeleton 27:1–12
73. Wessels D, Voss E, Von Bergen N, Burns R, Stites J, Soll DR (1998) A computer-assisted system for reconstructing and interpreting the dynamic three-dimensional relationships of the outer surface, nucleus and pseudopods of crawling cells. Cell Motil Cytoskeleton 41:225–246
74. Soll DR (1999) Computer-assisted three-dimensional reconstruction and motion analysis of living, crawling cells. Comput Med Imaging Graph 23:3–14
75. Hermann L (1976) Laplacian-isoparametric grid generation scheme. J Eng Mech Div 102:749–756